

Liquid argon scintillation response to electronic recoils between 2.8–1275 keV in a high light yield single-phase detector

M.Kimura*, K.Aoyama, M.Tanaka, K.Yorita

Waseda University, 3-4-1, Okubo, Shinjuku, Tokyo, 169-8555, Japan

Abstract

We measure the liquid argon scintillation response to electronic recoils in the energy range of 2.82 to 1274.6 keV. The single-phase detector with a large optical coverage used in this measurement yields 12.6 ± 0.3 (11.1 ± 0.3) photoelectron/keV for 661.7 keV γ -ray events based on a photomultiplier tube single photoelectron response modeling with a Gaussian plus an additional exponential terms (with only a Gaussian term). It is exposed to a variety of calibration sources such as ^{137}Cs and ^{241}Am γ -ray emitters, and ^{252}Cf fast neutron emitter that induces quasimonoenergetic γ -rays through a $(n, n'\gamma)$ reaction with ^{19}F in polytetrafluoroethylene. In addition, the high light yield enables identification of the 2.82 keV peak of ^{37}Ar , a cosmogenic isotope in atmospheric argon. The scintillation yield and energy resolution of the detector are obtained by the full-absorption peaks. We find up to approximately 25% shift in the scintillation efficiency across the energy range and less than 3% of the energy resolution for the 661.7 keV line. The energy dependent scintillation quenching can be attributed by the electron-ion recombination process, and is discussed by an analogy to the dependence of liquid xenon. The Thomas-Imel Box model with its constant parameter $\zeta = 0.07_{-0.02}^{+0.03}$ is found to explain the results below 200 keV.

Keywords: Liquid argon, Scintillation, Vacuum ultraviolet light, Dark matter

1. Introduction

A liquid argon (LAr) scintillation detector has several features that make it attractive for use in various physics experiments to detect ionization particles: it has efficient conversion of energy deposition into a scintillation light signal, powerful discrimination between electronic recoil (ER) and nuclear recoil (NR) events based on its scintillation pulse shape, and benefits from the fact that large quantities of argon are cheaply available. One promising application of the detector is to search and identify the NR signal possibly induced by a dark matter candidate, weakly interacting massive particles (WIMPs) [1, 2]. The typical energy of the signal is in the range of a few keV to several hundreds of keV. Burdensome backgrounds in this search are ER events caused by β -rays from diffused isotopes (such as ^{39}Ar and ^{85}Kr) in LAr and γ -rays from radio-impurities in detector components. Predicting the measured sig-

nal from these background sources is necessary to estimate its contamination in the signal region of interest. In this context, characterization of the detector response to ER events is crucial for achieving lower energy threshold, suppressing systematic uncertainty related to background contamination, and hence enhancing physics sensitivity of the search.

In the LAr detector, a charged particle interaction excites and ionizes the detector medium, resulting in the formation of self-trapped exciton states, Ar_2^* , through the collision and recombination processes. The excimer is formed in either a singlet or a triplet state, both of which decay radiatively with vast different lifetimes of approximately 7 ns and 1.6 μs , respectively [3]. The scintillation light spectra from both radiative decays lie in the vacuum ultraviolet (VUV), peaked at 128 nm [4]. As direct detection of the VUV photon at LAr temperature (around 87 K) is technically challenging, it is often downshifted to the visible region where most cryogenic photosensors exhibit peak sensitivity using a wavelength shifter such as 1,1,4,4-tetraphenyl-1,3-butadiene (TPB) [5, 6]. The recoiled particle and its energy are inferred from the observed photon signal

*Corresponding author.

Email addresses: masato@kylab.sci.waseda.ac.jp (M.Kimura), kohei.yorita@waseda.jp (K.Yorita)

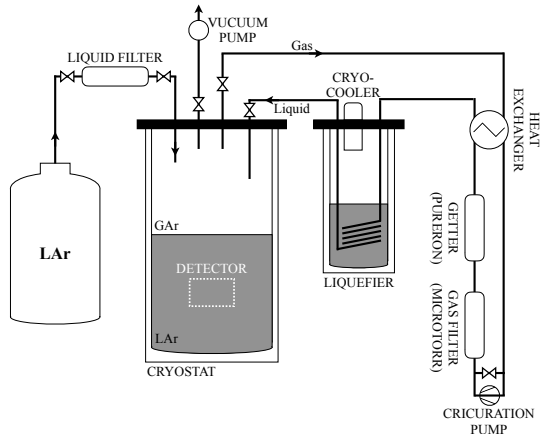


Figure 1: LAr handling system consisting of the filling line (left part of the schematic), the vacuum line (top center), the recirculation line (right), and the main cryostat (center). In the recirculation line, gaseous argon (GAR) extracted from the cryostat is pumped into the getters after passing through a heat exchanger. It then returns to the heat exchanger to be cooled and is condensed in the liquefier. The cryostat containing the detector maintains GAR and LAr over the data collection period in stable cryogenic conditions.

waveform.

In this work, we measure the LAr scintillation response to ER ranging from 2.82 to 1274.6 keV using a high light yield single-phase detector at null electric field. The measurement is performed with a variety of calibration sources including the 2.82 keV line of cosmic-ray induced ^{37}Ar . We present the energy dependence of the scintillation yield, as well as the basic properties of this detector such as the absolute scintillation light yield and energy resolutions of the full-absorption peaks. The energy dependence of the scintillation efficiency down to a few keV is discussed by comparing a model prediction, which is allowed by the use of the ^{37}Ar source.

2. Experimental apparatus

The measurement presented here is performed at the surface laboratory at Waseda University. Figure 1 shows the argon handling system used in this work. It mainly consists of a stainless-steel cryostat of diameter 50 cm and height 100 cm, in which a scintillation detector sits. The argon filled in the cryostat is cooled by the recirculation system, which extracts hot gas from the cryostat and passes it through the liquefier with a 200 W GM-cryocooler (SUMITOMO CH-110). The argon is maintained at a typical pressure of 1.4 atm and at a liquid level that varies by no more than 1 mm throughout the data collection period.

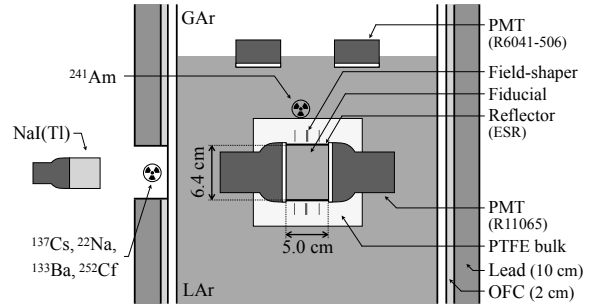


Figure 2: Schematic of the LAr scintillation detector (not scaled). The detector including the PMTs is immersed in LAr. Oxygen-free copper (OFC) of roughly 2 cm thick and lead of 10 cm thick surround the cryostat and act as a passive shield against ambient γ -rays. An ^{241}Am source is installed at the outer surface of the PTFE bulk, and the other sources (^{137}Cs , ^{22}Na , ^{133}Ba , and ^{252}Cf) are placed on the outside surface of the cryostat wall.

Impurities in the argon (such as water, oxygen, and nitrogen) affect the scintillation properties, resulting in a reduced signal yield [7–9]. In order to remove adsorbed impurities and outgassing from the detector components, the whole system is pumped to vacuum over about 10 days before the measurement. The pressure of the cryostat reaches below 1.0×10^{-3} Pa. Then commercial LAr fills the system via a single path through a liquid filter consisting of a molecular sieve and reduced copper which removes electronegative impurities. Additional purification is continuously performed by the getters (SAES MICROTORR MC1500-902 and PURERON GP-5) in the recirculation system. Several measurements performed in this system confirm the concentrations of these impurities are negligible in this measurement; water and oxygen contaminations of sub-ppb level and nitrogen contamination of sub-ppm level.

The scintillation detector, shown in Fig. 2, is designed to minimize the loss of scintillation photons in their path and maximize light-collection efficiency. The cylindrical fiducial volume of the detector has a diameter 6.4 cm and a length 5 cm, contained within an approximately 3 cm thick polytetrafluoroethylene (PTFE) sleeve. A multilayer plastic-foil reflector (3M ESR) lines the inner surface of the PTFE sleeve. Each end of the cylindrical volume is capped by 3-inch HAMA-MATSU R11065 photomultiplier tubes (PMTs), with around 30% of quantum efficiency (QE) for blue light. Since these PMTs are operated with a negative bias voltage of -1570 V, field-shaping rings with the same bias voltage are embed in the PTFE bulk and ensure electric field inside the fiducial volume less than 1 V/cm. The TPB wavelength shifter is deposited on both the reflec-

tor and the PMT windows using a vacuum-evaporation technique. The amounts of deposited TPB are approximately $40 \mu\text{g}/\text{cm}^2$ and $30 \mu\text{g}/\text{cm}^2$, respectively, corresponding to the deposited-layer thicknesses of $\mathcal{O}(1 \mu\text{m})$. These are confirmed by a quartz crystal microbalance sensor and a stylus profiler, as with a procedure similar to that reported in Ref. [10]. The whole of the sleeve is immersed in a LAr bath contained in the cryostat.

Four 2-inch PMTs (HAMAMATSU R6041-506) are implemented to view the LAr bath surrounding the fiducial volume, as shown in Fig. 2. These PMTs are located 20 cm above the fiducial volume and just below the liquid surface so that additional energy deposition in the outer region is tagged by a coincident scintillation signal. The windows of the PMTs are also coated with TPB. A passive shield against ambient γ -rays surrounds the cryostat, which consists of roughly 2 cm thick oxygen-free copper and 10 cm thick lead.

The data acquisition (DAQ) system used in this experiment consists of a 14-bit, 250 MS/s flash ADC (Struck SIS3316). The signals from two fiducial-viewing PMTs and four outer-bath PMTs are digitized and recorded. The length of the digitizer records is set to $25 \mu\text{s}$ ($5 \mu\text{s}$ before a trigger point and $20 \mu\text{s}$ after), longer enough than the lifetime of the slow component of LAr scintillation light. The trigger is given by the coincidence, within $1 \mu\text{s}$, of the two fiducial PMTs with pulses above a threshold, which is set just above the baseline noise and below a typical single photoelectron (p.e.) pulse. The coincidence decision is internally made by the flash ADC board itself. An inhibition time of $100 \mu\text{s}$ is introduced after each trigger to prevent re-triggering of the afterpulse of the PMTs, which mainly occurs after events with far greater energies than the region of interest (e.g., cosmic-ray events). A Monte Carlo (MC) simulation of the LAr data sample is generated to evaluate the trigger efficiency. By emulating the internal trigger logic of the flash ADC board on these MC events, the efficiency is found to be consistent with unity for ER signals larger than 25 p.e., as shown in Fig. 10.

3. Event analysis

3.1. PMT calibration

The gain of the fiducial PMTs is calibrated using a blue LED powered by a pulse generator. Light pulses from the LED, characterized by a width of approximately 20 ns at tenth maximum, are injected into the fiducial volume through optical fiber, while the generator simultaneously triggers the DAQ system and the corresponding waveforms from each PMT are recorded

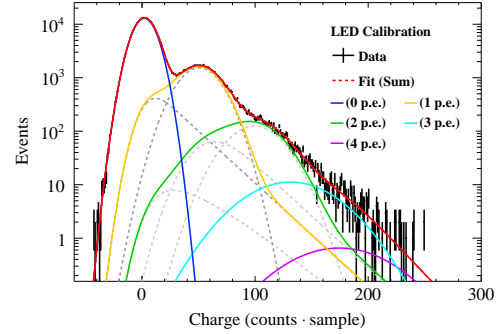


Figure 3: A typical low-light charge distribution of a fiducial-viewing PMT from an LED calibration run. The charge is represented in units of integrated digitizer count (count · samples), where 1 count · sample corresponds to 9.8×10^{-15} C. The solid red line is the model fit as expressed in Eq.(1), and the colored thin lines represent its components.

over a window of $\pm 1 \mu\text{s}$. A baseline ADC count is determined by the first $0.6 \mu\text{s}$ of the window, and its subtraction is applied waveform-by-waveform. The charge response of the PMT is measured by integrating the waveforms within a 48 ns window starting 20 ns prior to the photoelectron pulse arrival time. The gain value is determined by fitting the charge distribution to model functions. In this analysis, two models are considered to describe the PMT response. One expression of the models (Gain-Model A) as a function of the integrated charge q is followed to that used in Ref. [11]:

$$\begin{aligned}
 f(q) &= \sum_n P(n; \lambda) \times f_n(q), & (1) \\
 f_n(q) &= \rho(q) * \psi_1^{n*}(q), \\
 \rho(q) &= G(q; x_0, \sigma_{\text{ped}}), \\
 \psi_1(q) &= \frac{p_E}{\tau} \exp(-q/\tau) + (1 - p_E)G(q; x_m, \sigma_m)
 \end{aligned}$$

where $P(n; \lambda)$ is a Poisson distribution with mean λ , $G(q; x, \sigma)$ is a Gaussian distribution with mean x and standard division σ , $*$ denotes a convolution, $\psi_1(q)$ is the PMT single photoelectron response, and $\psi_1^{n*}(q)$ is the n -fold convolution of $\psi_1(q)$ with itself. This model consists of two components comprising the PMT response: a simple Gaussian term, which accounts for a photoelectron signal fully amplified by the dynode chain, and an exponential term characterized by a parameter τ , which accounts for under-amplified photoelectrons and/or feedback from the dynode photoemission signal. The fraction of the single photoelectron response found to be the under-amplified terms is p_E . Another expression (Gain-Model B) is simpler, consisting of only the Gaussian term; i.e., the fraction p_E in Eq.

(1) is fixed to 0. This assumes that there is no under-amplified or dynode-feedback response in a PMT and that the photoelectron response is perfectly described by Gaussians.

Figure 3 shows the charge distribution and fit for an LED calibration run with the Gain-Model A (which has a non-zero fraction p_E), where 1 count · sample corresponds to an output charge of 9.8×10^{-15} C. The mean charge for a single photoelectron g , defined as

$$g = p_E \tau + (1 - p_E) x_m, \quad (2)$$

is approximately $2.0 \times 10^6 e^-/\text{p.e.}$ with a bias voltage of -1570 V. The fit with the Gain-Model B (i.e., simple convolution of Gaussian functions) returns a 12% higher gain value than Gain-Model A. This difference is nearly consistent with the result reported in Ref. [11]. While we do not have enough data to determine which model is more appropriate to describe the PMT response, the Gain-Model A is adopted as baseline and the result from the model is used in the later analysis. This calibration is performed every 12 hours during a data collection period lasting 7 days. No significant time dependences of the gain are observed for the two PMTs.

3.2. Signal analysis and selection criteria

The analysis of the LAr scintillation signal is performed following a photoncounting algorithm. For each waveform, this algorithm first calculates the baseline from the pre-trigger window; once that baseline is subtracted, all samples above a software threshold are grouped with three neighboring samples (1 bin before and 2 bins after). The software threshold is set based on the baseline noise and is below a typical single photoelectron PMT pulse. The signal detection time is identified as the first sampling time above a threshold of 50% peak amplitude. Detected scintillation light is defined as the integrated charge in the time interval between -0.04 and $7.0 \mu\text{s}$. A pulse shape discrimination (PSD) parameter is also defined as the fraction of light detected after $0.1 \mu\text{s}$ of the scintillation signal (termed “Slow/Total”).

A set of data quality cuts is applied to remove instrumental effects and event pileups. The selection criteria are as follow. (1) Software imposes a 10 ms veto after events that contain signals greater than $\approx 2.0 \times 10^4$ ($\approx 5.0 \times 10^3$ p.e.) for datasets taken with a γ -ray source with >100 keV (<100 keV) its energy. This aims to remove the unstable period of the PMT after outputting a large charge signal. (2) The event has a stable baseline noise and no more than 0.7 p.e. pulses in the pre-trigger window. (3) The sum of the pulses present after the signal-integration window is consistent within about four times its expectation. (4) The

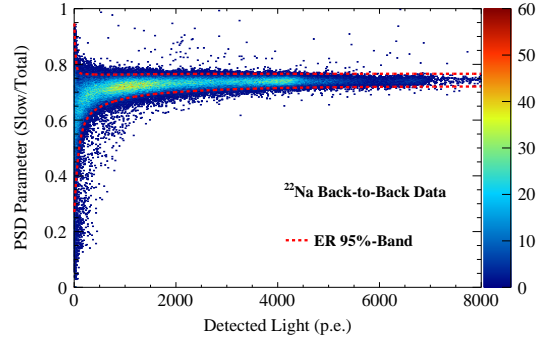


Figure 4: Distribution of the PSD parameter (“Slow/Total”) versus the scintillation signal. The data requires the back-to-back tagging described in Sec. 4.1. The red dashed lines correspond to the 95% containing band for ER events.

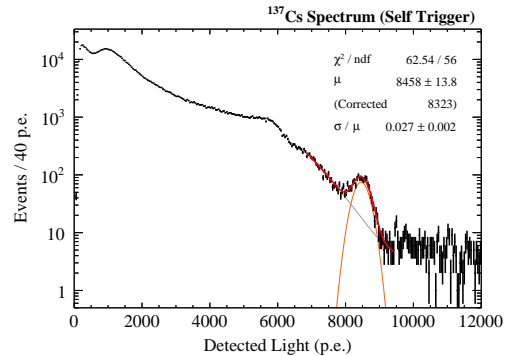


Figure 5: The scintillation spectrum from the ^{137}Cs source used for the energy calibration. The red lines represent the fit function.

event does not occur near the PMT and is more likely to be a LAr scintillation signal than Cherenkov light on the PMT window. The signal asymmetry, defined as $A = (N_{\text{p.e.}}^1 - N_{\text{p.e.}}^2) / (N_{\text{p.e.}}^1 + N_{\text{p.e.}}^2)$ in which $N_{\text{p.e.}}^1$ and $N_{\text{p.e.}}^2$ are the observed photoelectron signal in each PMT, is used to evaluate the interacting position. The cut value is selected to contain approximately 99% of the LAr signal. (5) The PSD parameter of the event is consistent with that of the ER. The band of the parameter used in this cut is determined by ^{22}Na data to contain 95% of ER events, as shown in Fig. 4.

3.3. Energy calibration with a Cesium-137 source

Energy calibration of the detector is performed using a ^{137}Cs γ -ray source placed on the outside surface of the cryostat wall. Figure 5 shows the observed scintillation spectrum obtained with the source. The full-absorption peak of the 661.7 keV line of the ^{137}Cs source is fit with a Gaussian with mean μ and width

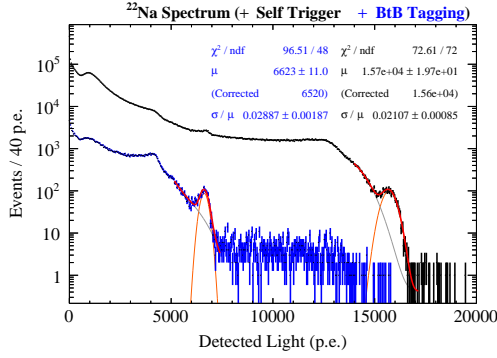


Figure 6: The scintillation spectra from the ^{22}Na source, before and after requiring back-to-back coincidence (BtB tagging). The red lines represent the fit function.

σ . The continuous background components around the peak, mainly coming from the Compton edge and degraded tails, are modeled with error and linear functions and added to the fit function. The fit shown in Fig. 5 returns $\chi^2/ndf = 62.5/56$. It is monitored every day throughout the data collection period, and no significant time dependence is observed.

The observed light yield obtained in Fig. 5 contains extra charge from PMT afterpulses and systematic effect from the photoncounting algorithm. A correction for these effects is thus applied to reconstruct the observed light yield per ER energy. This correction is based on an independent study of the PMT response as well as a MC simulation of the LAr signal. It is relatively small, approximately 1% for the ^{137}Cs line and less than 3% for the whole of energy region of interest of this analysis, where the amount of afterpulse is estimated 2%–4% of the photoelectron signal and the algorithm can systematically slightly underestimate the charge signal. The resulting light yield is 12.6 ± 0.3 p.e./keV (11.1 ± 0.3 p.e./keV) when using the PMT calibration obtained by the Gain-Model A (Gain-Model B). The uncertainty includes the estimation of PMT afterpulses, systematic error in the correction, and variance of the light yield between daily calibrations.

4. Measurement of scintillation response with calibration sources

4.1. Sodium-22 source

The detector is exposed to 511.0 and 1274.6 keV γ -rays using a ^{22}Na radioactive source of approximately 1 MBq. The source is placed near the cryostat wall with an NaI(Tl) scintillator (2 inch \times 2 inch cylinder). This

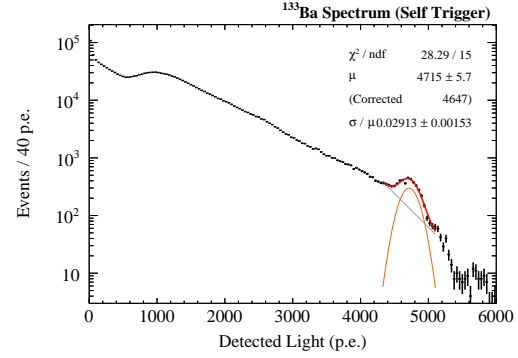


Figure 7: The scintillation spectrum from the ^{133}Ba source. The red line represents the fit function.

additional scintillator is located opposite to the site of the cryostat to tag the backwards-traveling 511.0 keV γ -ray (back-to-back tagging). The distance between the cryostat wall and the source is set to 15 cm, and that between the source and the scintillator to 25 cm. Figure 6 shows the scintillation spectra obtained with the ^{22}Na source before and after requiring the coincidence detection of the 511.0 keV γ -ray signal in the NaI(Tl) scintillator. Since the 1274.6 keV γ -ray is considered to have no angular correlation with back-to-back γ -rays, the corresponding peak appears only in the former spectrum. Each peak is fit with a Gaussian plus background model function consisting of error and linear functions, as overlaid in Fig. 6.

4.2. Barium-133 source

The detector is exposed to 356.0 keV γ -ray using ^{133}Ba radioactive source with approximately 1 MBq. The spectrum obtained with a ^{133}Ba source is shown in Fig. 7. The peak around 4700 p.e. corresponds to the γ -ray line and fitted with a Gaussian. An exponential function is added to the fit function to model the overall background components; the main background sources are due to the degraded γ -ray tail and the γ -ray spectra of the other two lines of the ^{133}Ba source around the peak energy (those at 383.9 keV and 302.9 keV) that have relatively high intensity. The resulting fit function is overlaid in Fig. 7.

4.3. Californium-252 source exploiting γ -rays through the $(n, n'\gamma)$ reaction with fluorine-19

Measurements of the scintillation responses for the 109.8 and 197.1 keV quasimonoenergetic lines are performed using γ -rays emitted from the $(n, n'\gamma)$ reaction with ^{19}F [12]. As an external fast neutron source, a

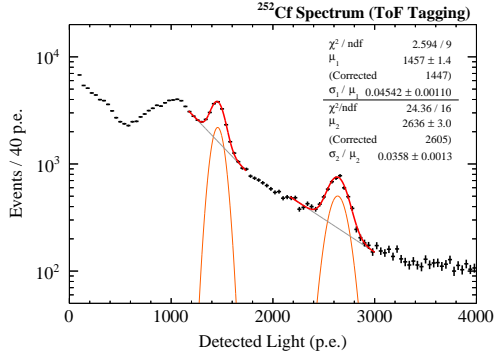


Figure 8: The scintillation spectrum from the ^{252}Cf source after requiring the ToF to be consistent with fast neutrons. The red lines represent the fit function.

^{252}Cf source with a spontaneous fission rate of approximately 1×10^5 fission/s is used. The distance between the center of the fiducial volume and the source is set to 90 cm. The NaI(Tl) scintillator is placed beside the source to detect associated γ -rays from the spontaneous fission and to provide timing information. Fast neutrons from ^{252}Cf generate $(n, n'\gamma)$ reaction with ^{19}F in the PTFE bulk, producing quasimonoenergetic γ -rays. Although the intensities of each quasimonoenergetic line depend upon their incident neutron energy, 109.8 and 197.1 keV lines are major channels for the range of neutron energy from ^{252}Cf . Time differences between the NaI(Tl) and fiducial signals (time of flight; ToF) are used to remove γ -ray events that come directly from the fission. Figure 8 shows the spectrum and fitting results for corresponding peaks. Each peak is fit by a Gaussian plus exponential function.

4.4. Americium-241 source

To expose the detector to 59.5 keV γ -rays, an ^{241}Am source of approximately 40 Bq is used. The radioactive source is deposited on a 100 μm thick platinum foil installed at the outer surface of the PTFE bulk. It decays into an excited level of ^{237}Np via α -ray transition, and subsequent de-excitation of the ^{237}Np emits γ -rays with a major line of 59.5 keV. The α -ray from the primary disintegration is detected by the outer-bath PMTs, allowing the γ -ray interaction to be proved in the fiducial volume. Figure 9 shows the scintillation spectrum after requiring the detection of α -ray signals in the outer region. Due to the relatively low energy of the γ -ray from ^{241}Am and the passive components between the source and the fiducial volume, the spectrum does not exhibit a clear full-absorption peak. The tail of the peak comes

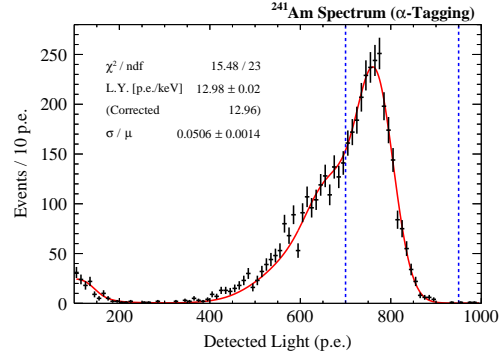


Figure 9: The scintillation spectrum from the ^{241}Am source by requiring α -ray detection by the veto PMTs, along with the MC fit spectrum (red line). The blue dashed vertical lines represent the fitting range.

from γ -rays that reach the fiducial volume via single or multiple scattering from any materials in their path.

The scintillation response to a 59.5 keV γ -ray is evaluated via MC simulation of the experimental setup based on the Geant4 toolkit [13, 14]. The MC simulation takes into account the detector geometry and composition inside the LAr bath, as well as the radioisotope mounting structure. It proceeds by generating γ -rays from ^{241}Am with a random momentum direction and calculating the energy deposition in the fiducial volume. The fit of the energy deposition spectrum to the ^{241}Am data provides the scintillation efficiency for 59.5 keV γ -rays. This fit is performed by converting the energy deposition to the observed scintillation yield with a constant scintillation efficiency and Gaussian resolution. The best fit spectrum is also shown in Fig. 9; although the fit is performed only around the 59.5 keV peak (700–900 p.e.), reasonable agreement between data and MC is found down to around 400 p.e.

4.5. Argon-37 source

Measurement for ERs of a few keV is performed using ^{37}Ar , which is the second most abundant radioactive isotope in atmospheric argon, comprising an abundance of $\approx 1.3 \times 10^{-20}$ [15]. It decays via electron capture to the ground state of ^{37}Cl with a half-life of 35 days, producing x-rays and Auger electrons with a total energy release of 2.82 keV (for K-shell capture), 0.27 keV (for L-shell capture), or 0.02 keV (for M-shell capture) [16, 17]. Since the production of ^{37}Ar is mainly due to cosmogenic activation of atmospheric argon [15], it is expected to reach equilibrium and the decay rate of ^{37}Ar in the detector is expected to be constant from the argon filling time to the end of measurement.

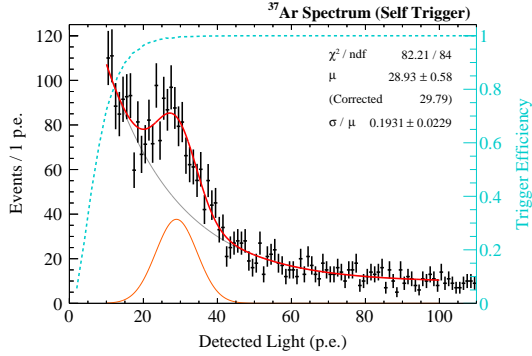


Figure 10: The ^{37}Ar spectrum obtained by requiring anti-coincidence with the outer bath PMTs for the no external source data. The cyan dashed line represents the estimated trigger efficiency and the data is corrected based on this curve.

The data used in this measurement come from approximately 27 hours of detector operation without any external sources. Figure 10 shows the scintillation spectrum for this measurement. The spectrum consists of events that do not have associated scintillation signals in any of the four outer-bath PMTs. The peak around 25 p.e. is attributed to the energy release of 2.82 keV from ^{37}Ar . No structures corresponding to the L- or M-shell capture could be seen, probably due to the large amount of random coincidence background and the lack of photostatistics. The spectrum with ^{37}Ar is fitted with the sum of the Gaussian, exponential, and constant terms that describes the signal and low energy background model. The rate of ^{37}Ar decays returned by the fit is approximately 25 mBq/kg, which is compatible with literature values [15, 18, 19]. The goodness of fit for the peak is $\chi^2/ndf = 82.21/84$.

5. Scintillation yield and energy resolution

The upper panel of Fig. 11 summarizes the mean values of the number of detected photoelectron divided by corresponding incident energies, measured by the set of radioactive sources described in the previous section. Nonlinear response on the scintillation yield is seen, which peaks around 200 keV. This trend can be attributed to the energy dependence of the ionization electron-ion recombination probability. The Thomas-Imel Box (TIB) model [20] and Doke-Birks' law [21] can presumably explain the data, as is the case for the liquid xenon (LXe) scintillation detector [22]. For higher energy range, the Doke-Birks' law is generally applied to deal with relativistic and longer range tracks and to predict the decrease of the probability as the track

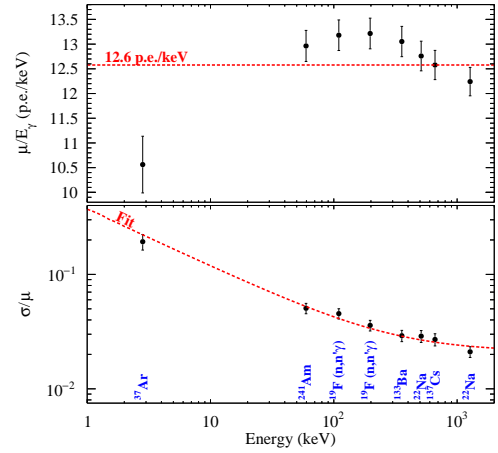


Figure 11: (Top) Peak scintillation yields obtained by the fitting analysis for each calibration line, divided by corresponding incident energy. The red dashed line represents the energy calibration using 661.7 keV full-absorption peak. (Bottom) Energy resolution of the detector measured with full-absorption peaks. The red dashed line represents the fit function with stochastic and constant terms (see text).

energy increases (or dE/dx decreases). On the other hand, for lower energy range, typically less than several hundred keV, it is known that the TIB model is suitable for modeling the data because it is based on the low energy recoiled track whose range is comparable to or shorter than the mean ionization electron-ion thermalization distance. In the following section, we focus on the scintillation response in lower energy range, less than 200 keV, and thus employ the TIB model to explain our data. Further study for quantitative evaluation and its modeling of the response will be discussed in

Table 1: Observed coefficients and estimated contributions of the stochastic (S) and constant (C) terms of the energy resolution. Although the origin of the constant term is not quantitatively estimated, almost all of which is believed to come from the geometrical effect.

Type	Source	Coefficient (α)
S ($\frac{\sigma}{\mu} = \frac{\alpha}{\sqrt{E_\gamma}}$)	Data	0.37 ± 0.03
	Photostatistics	≈ 0.3
	Multiple scattering	< 0.1
	PMT gain and afterpulse	$\lesssim 0.2$
	Photoncounting algorithm	≈ 0.0
	TPB wavelength shift	0.0–0.1
C ($\frac{\sigma}{\mu} = \alpha$)	Data	0.021 ± 0.002
	Geometrical effect	(≈ 0.02)

Table 2: Summary of the systematic uncertainty sources for the measurements of the scintillation yields and energy resolution.

Systematic	Scintillation yields		Energy resolution	
	Dataset	Fraction	Dataset	Fraction
PMT afterpulse	all	2.0%		
Time stability of the detector	all	0.5%		
Photoncounting algorithm	all	1.0%		
Function modeling	^{241}Am	0.8%	all	10%
	others	0.5%		
Trigger efficiency	^{37}Ar	4.5%		
	others	0		

Sec. 6.

The energy resolution of the detector is also characterized based on the full-absorption peaks and is shown in the lower panel of Fig. 11. The set of points is fit to the function

$$\frac{\sigma}{\mu} = \sqrt{\frac{\sigma_s^2}{E_\gamma} + \sigma_c^2}, \quad (3)$$

where σ_s accounts for stochastic fluctuation and σ_c accounts for the variance of the mean value of mono-energy deposition. The values are found to be $\sigma_s = 0.37 \pm 0.03$ and $\sigma_c = 0.021 \pm 0.002$, respectively.

Several sources are expected to degrade the energy resolution. The contribution of each source are examined and listed in Table 1. Upon examination, it is clear that the statistical fluctuation for the scintillation process is the dominant source of the stochastic term (σ_s/E_γ), where it is assumed as Poissonian. Convoluting the terms listed in Table 1 explains approximately 90% of the stochastic term observed in the data; the rest of the term is currently unknown. The constant term (σ_c) is believed to mainly consist of the geometrical effect. We should note that the scintillation process is suggested to have a smaller fluctuation than that would be expected under the Poissonian assumption due to the Fano effect [23]; however, this measurement has little sensitivity to this, due to the small light-collection efficiency (roughly 30%, which is mainly limited by the PMT QE) and the relatively large degradation of the resolution from other sources.

The result is subjected to several systematic uncertainty sources which stem from both the detector response and the analysis procedure, as listed in Table 2. The former is the PMT afterpulse, explored by the PMT response study using both LAr data and a property measurement after the LAr detector operation, and the time stability of the detector complex, monitored by the regular calibrations throughout the data collection period.

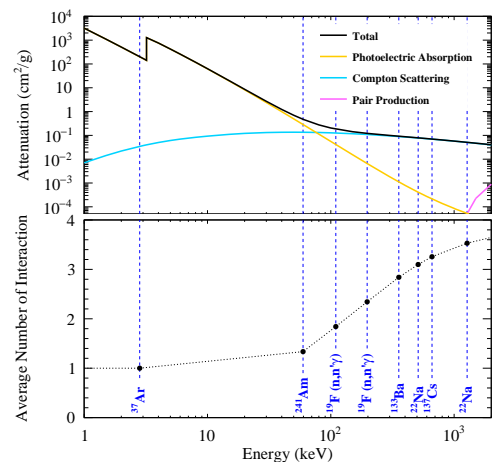


Figure 12: (Top) The γ -ray cross sections for argon provided by XCOM [24]. (Bottom) Average number of interaction points for the full-absorption peaks calculated by the Geant4 MC simulation.

The later mainly comes from the photoncounting algorithm part and the related correction of the analysis. We assign the size of the correction as the uncertainty. Relatively small uncertainty is attributed to the fit of the full-absorption peak, which is estimated by refitting the peak with a simple Gaussian function. The trigger efficiency is an additional uncertainty source for the ^{37}Ar line analysis. We refit the peak without the correction, and assign the corresponding uncertainty as the variation between these results.

The uncertainty of the energy resolution is considered as typically 10% in total, mainly from the fitting modeling.

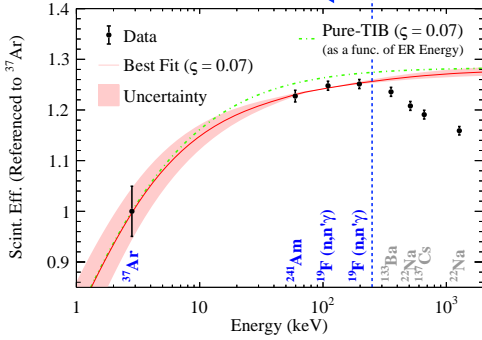


Figure 13: Measured scintillation efficiencies as a function of the incident energy E_γ . The data points below 200 keV (indicated by the blue dashed line and arrow) is fit to the TIB model and Geant4 MC simulation (red solid line and band). The TIB model function with the same parameter, as a function of the electron energy E_{er} , is also shown for the purpose of indicating the multi-scattering effect (green dot-dashed line).

6. TIB model interpretation on scintillation response

As discussed in the previous sections the measurable quantity in this analysis is the scintillation yield, defined as the detected photoelectron signal of the full-absorption peak divided by the corresponding incident energy, E_γ . On the other hand, the scintillation efficiency is expected to depend on the recoiled electron energy, not directly on the selected full-absorbed γ -ray energy because of multiple scattering inside the fiducial volume. Thus we should note that the definition of the real interaction energy (averaged energy) depends on the geometry and size of the detector. In fact the γ -ray cross section for argon (upper panel of Fig. 12) [24] and the average number of the interaction points for each calibration point calculated by a Geant4 MC simulation (lower panel of Fig. 12) indicate that our selected full-absorbed events generally have one or more interaction points by Compton scattering before photoelectric absorption inside the fiducial volume. As the incident γ -ray energy increases, the Compton scattering cross section and thus the number of the interaction increase accordingly. Therefore, for the higher energy points, contributions from lower energy recoiled electron to the total deposited energy have to be considered to determine invariant quantity for interaction energy. In the following, since the number of the interaction point of the ^{37}Ar events is one due to its low energy deposition and decay mode mainly consisting of Auger electrons [16], all the data points are normalized by the response of the ^{37}Ar and the effect of multiple scatter-

ing for each energy point is estimated and corrected by using the Geant4 MC simulation and TIB model:

$$n_{ph} = \frac{E_{er}}{W}(N_{ex} + rN_i) = \frac{E_{er}}{W} \frac{1+r}{1+\alpha}, \quad (4)$$

$$r = 1 - \frac{1}{N_i\zeta} \ln(1 + N_i\zeta),$$

which predicts the number of produced scintillation photons, n_{ph} , for recoil electron energy E_{er} . In Eq. (4), $W = 19.5$ eV is the effective work function [21], N_{ex} and N_i are the numbers of produced excitons or electron-ion pairs, respectively, $\alpha = 0.21$ is the initial ratio of the average of N_{ex} to N_i [25], and ζ is a constant parameter of the model. Parameter ζ in the TIB model is evaluated by fitting the measured points below 200 keV to the MC simulation as shown in Fig. 13. The fit returns a value of $\zeta = 0.07^{+0.03}_{-0.02}$, where the uncertainty includes both statistical and systematical terms. The shift of the scintillation efficiency for the same energy of full-absorbed γ -ray (red solid line of Fig. 13) and single electron track (green dot-dashed line) is estimated as 2%–3% around 100 keV in this detector. The TIB model reasonably explains our data up to 200 keV by taking into multiple scattering effect account.

7. Conclusion

The energy dependence of the scintillation efficiency for electronic recoils ranging from 2.82 to 1274.6 keV is measured using a single-phase high light yield detector exposed to a variety of calibration sources. The scintillation detector with the TPB wavelength shifter is immersed in purified LAr and yields 12.6 ± 0.3 p.e./keV (11.1 ± 0.3 p.e./keV) based on the PMT calibration assuming a PMT single photoelectron response model with an additional exponential term (with only Gaussian term). The LAr scintillation response is investigated by the full-absorption peaks of external γ -ray sources, as well as an ^{37}Ar source with 2.82 keV line. These measurements demonstrate that the efficiency peaks at around 200 keV and energy resolution is found to be less than 3% for the 661.7 keV γ -ray. In order to provide an invariant property of the LAr scintillation response, we investigate the scintillation quenching by analogy with the LXe scintillation detector response, where the electron-ion recombination probability is attributed to the energy dependence of the response. For the energy below 200 keV, the TIB model provides a good description of the observed scintillation quenching by the parameter ζ , and we obtain it as $\zeta = 0.07^{+0.03}_{-0.02}$.

This work is primary intended for use in the direct WIMP dark matter search. In this field, low energy

electronic background is one of the most severe sources disturbing the lower energy threshold, hence reducing WIMP sensitivity. The result presented here makes use of the precise estimation of background contamination in the low energy region and suppression of the systematic uncertainty. In addition, the measurement of the energy resolution for the keV to MeV range in this work provides useful information for applying the LAr detector to other fields, such as astrophysical MeV Gamma-ray observation [26]. The results presented here would help with the design, operation, and analysis of a wide variety of astrophysical and particle physics experiments in the near future to enhance their physical reach.

Acknowledgments

This work is a part of the outcome of research performed under the Waseda University Research Institute for Science and Engineering (project number 2016A-507), supported by JSPS Grant-in-Aid for Scientific Research on Innovative Areas (15H01038/17H05204), Grant-in-Aid for Scientific Research(B) (18H01234), and Grant-in-Aid for JSPS Research Fellow (18J13018). The authors would like to thank the Material Characterization Central Laboratory at Waseda University for granting us access to their stylus profiler. The authors acknowledge the support of the Institute for Advanced Theoretical and Experimental Physics, Waseda University.

References

- [1] P. Agnes *et al.*, Phys. Rev. D 98 (2018) 102006.
- [2] P.-A. Amaudruz *et al.*, Phys. Rev. Lett. 121 (2018) 071801.
- [3] A. Hitachi *et al.*, Phys. Rev. B 27 (1983) 5279–5285.
- [4] T. Heindl *et al.*, Europhysics Letters 91 (6) (2010) 62002.
- [5] W. M. Burton, B. A. Powell, Appl. Opt. 12 (1) (1973) 87–89.
- [6] G. Porter, M. R. Topp, Proceedings of the Royal Society of London. A. Mathematical and Physical Sciences 315 (1521) (1970) 163–184.
- [7] R. Acciarri *et al.*, J. Instrum. 5 (05) (2010) P05003.
- [8] R. Acciarri *et al.*, J. Instrum. 5 (06) (2010) P06003.
- [9] B. J. P. Jones *et al.*, J. Instrum. 8 (12) (2013) P12015.
- [10] B. Broerman *et al.*, J. Instrum. 12 (04) (2017) P04017.
- [11] T. Alexander *et al.*, Astroparticle Phys. 49 (2013) 44 – 51.
- [12] V. C. Rogers, Phys. Rev. C 9 (1974) 527–530.
- [13] S. Agostinelli *et al.*, Nucl. Inst. & Meth. in Phys. Res. A 506 (3) (2003) 250 – 303.
- [14] J. Allison *et al.*, IEEE Trans. Nucl. Sci. 53 (1) (2006) 270–278.
- [15] R. Saldanha *et al.*, Phys. Rev. C 100 (2019) 024608.
- [16] B. T. Cleveland *et al.*, Astrophys. J. 496 (1) (1998) 505–526.
- [17] M.-M. Bé *et al.*, Table of Radionuclides, Vol. 7 of Monographie BIPM-5, Bureau International des Poids et Mesures, Pavillon de Breteuil, F-92310 Sèvres, France, 2013.
- [18] R. Purtschert *et al.*, in: CTBT Science and Technology 2017 Conference (CTBT, Vienna, 2017), 2017, sec. T1.3-O2.
- [19] P. Agnes *et al.*, Phys. Rev. Lett. 121 (2018) 081307.
- [20] J. Thomas, D. A. Imel, Phys. Rev. A 36 (1987) 614–616.
- [21] T. Doke *et al.*, Nucl. Inst. & Meth. in Phys. Res. A 269 (1) (1988) 291 – 296.
- [22] M. Szydagis *et al.*, J. Instrum. 6 (10) (2011) P10002.
- [23] T. Doke *et al.*, Nucl. Inst. & Meth. 134 (2) (1976) 353 – 357.
- [24] M. Berger *et al.*, XCOM: Photon cross sections database (2010).
URL <https://www.nist.gov/pml/xcom-photon-cross-sections-database>
- [25] M. Miyajima *et al.*, Phys. Rev. A 9 (1974) 1438–1443, and Phys. Rev. A 10 (1974) 1452.
- [26] T. Aramaki *et al.*, Astroparticle Phys. 114 (2020) 107 – 114.